How many vent fields? New estimates of vent field populations on ocean ridges from precise mapping of hydrothermal discharge locations

Edward T. Baker[a,b,*], Joseph A. Resing[a,b], Rachel M. Haymon[c], Verena Tunnicliffe[d], J.William Lavelle[b], Fernando Martinez[e], Vicki Ferrini[f], Sharon L. Walker[b], and Koichi Nakamura[g]

[a] Joint Institution for the Study of the Atmosphere and Ocean, University of Washington, Seattle WA 98105 USA (edward.baker@noaa.gov; joseph.resing@noaa.gov)

[b] NOAA/Pacific Marine Environmental Laboratory, 7600 Sandpoint Way NE, Seattle, WA 98115 USA (sharon.l.walker@noaa.gov)

[c] Department of Earth Science and Marine Science Institute, 2031 Webb Hall, University of California, Santa Barbara, CA 93106 USA (haymon@geol.ucsb.edu)

[d] School of Earth & Ocean Sciences and Department of Biology, BWC A325, University of Victoria, Victoria, B.C. V8W 3N5 Canada (verenat@uvic.ca)

[e] University of Hawai'i at Manoa, Hawai'i Institute of Geophysics and Planetology, 1680 East-West Road, POST 814A, Honolulu, HI 96822 USA (fernando@hawaii.edu)

[f] Lamont-Doherty Earth Observatory, 75 Geoinformatics Center, 61 Route 9W, Columbia University, Palisades, NY 10964 USA (ferrini@ldeo.columbia.edu)

[g] National Institute of Advanced Industrial Science and Technology, Tsukuba Central 7, 1-1-1 Higashi, Tsukuba, Ibaraki 305-8567 Japan (koichi.nakamura@aist.go.jp)

* Corresponding author

Abstract

Decades of exploration for venting sites along spreading ridge crests have produced global datasets that yield estimated mean site spacings of ~12–220 km. This conclusion demands that sites where hydrothermal fluid leaks from the seafloor are improbably rare along the 66,000 km global ridge system, despite the high bulk permeability of ridge crest axes. However, to date, exploration methods have neither reliably detected plumes from isolated low-temperature, particle-poor, diffuse sources, nor differentiated individual, closely spaced (clustered within a few kilometers) sites of any kind. Here we describe a much lower mean discharge spacing of 3–20 km, revealed by towing real-time oxidation-reduction-potential and optical sensors continuously along four fast- and intermediate-rate (>55 mm/yr) spreading ridge sections totaling 1470 km length. This closer spacing reflects both discovery of isolated sites discharging particle-poor plumes (25% of all sites) and improved discrimination (at a spatial resolution of ~1 km) among clustered discrete and diffuse sources. Consequently, the number of active vent sites on fast- and intermediate-rate spreading ridges may be at least a factor of 3–6 higher than now presumed. This increase provides new quantitative constraints for models of seafloor processes such as dispersal of fauna among seafloor and crustal chemosynthetic habitats, biogeochemical impacts of diffuse venting, and spatial patterns of hydrothermal discharge.

Keywords: **Hydrothermal venting, diffuse flow, ocean ridges, faunal distribution, geochemical budgets, crustal circulation**

1. Introduction

Hydrothermal circulation is the dominant global agent for the transfer of heat, chemicals, and microbial life from the upper lithosphere to the ocean. The global fluxes of hydrothermal heat, hydrothermal fluids, and some (mostly conservative) hydrothermal chemical species from the neovolcanic zone of ocean spreading ridges (OSRs) are reasonably well estimated (e.g., Elderfield and Schultz, 1996). However, for many biological, chemical, and physical processes at the crust-ocean interface, a key variable in assessing the role of hydrothermal discharge is the number and spacing of distinct discharge sites ("vent fields") along the 66,000 km of OSRs. The spacing of hydrothermal oases is critical to understanding the dispersal of chemosynthetic fauna (McGillicuddy et al., 2010; Vrijenhoek, 2010; Beaulieu et al., 2015) and recruitment success after ecosystem disruptions such as seabed mining (Hilário et al., 2015) and seafloor eruptions. Interest in the nature and number of low-temperature (<~50°C), diffuse venting sites, especially those isolated from sites of higher-temperature discrete venting, is increasing because Fe may be preferentially supplied to the ocean interior by diffuse discharge (German et al., 2015; Larson et al., 2015). Furthermore, the location of seafloor discharge provides our only direct information on the distribution of hydrothermal upflow sites, and thus on the pattern of hydrothermal circulation in the shallow crust (Hasenclever et al., 2014).

Thirty-five years of exploration has yielded an inventory of >500 active discharge sites on OSRs (Beaulieu et al., 2013, 2015). These and other inventories rely on published descriptions of discharge sites, which commonly lump closely spaced sites (e.g., within 10 km; Hannington et al., 2011) into a single named site. Beaulieu et al. (2015) used these data to predict a total of ~1300±600 sites on OSRs. This prediction implies a mean site spacing ranging from 25 km at ultrafast spreading rates (150 mm/yr) to 90 km at ultraslow rates (10 mm/yr). Similarly, Hannington et al. (2011) calculated that the spacing between 70 massive sulfide deposits on OSRs ranges from 10–330 km over the entire spreading rate range, roughly increasing with decreasing spreading rate.

However, direct evidence from crustal measurements and seafloor observations challenges the perception that vent fields are widely separated. Borehole measurements imply that the uppermost layer of very young crust is fractured and open, with bulk permeability as high as 10^{-10} m^2 (Fisher and Becker, 2000). This permeability is seemingly inconsistent with spacings of tens of kilometers between discharge sites, especially along ridge sections underlain almost continuously with an axial melt lens. Visual surveys along ridge crests at length scales of 10–100 km are rare, but where available show that discharge sites are far more common than implied by the global statistics (Haymon et al., 1991; Auzende et al., 1996; O'Neill, 1998; Haymon and White, 2004).

We propose that the disagreement between these two views of hydrothermal site spacing is a product of sampling strategy and sensor capability. Mapping of discharge sites at the globally relevant 100–1000 km scale is based almost exclusively on the detection of dispersing, non-buoyant, hydrothermal discharge (e.g., German and Parson, 1998; Baker and German, 2004). Observations are occasionally continuous over several ridge segments (German and Parson, 1998; Baker et al., 2006) but more generally use discrete sampling at intervals of several to tens of kilometers (Son et al., 2014). In either case, mapping of discharge plumes predominantly relies on the detection of broadly dispersing, conservative (e.g., ^{3}He, temperature) or quasi-conservative (e.g., optical, particulate Fe, dissolved Mn, CH_4) tracers that can be detected many kilometers from their source. These tracers are highly sensitive to particle-rich, "black smoker" discharge, generally at temperatures >~100°C, but their broad dispersion makes it difficult to distinguish closely spaced sites with comingling plumes. Detecting isolated discharge with a negligible particle or dissolved metal signature (e.g., Lost City; Larson et al. (2015)), or with disorganized flow that inhibits plume rise, is more problematical. Discrete sampling is apt to miss small sites, and temperature anomalies from such sites are commonly too weak to be reliably detected during a tow. In this paper, we use continuous tows of a sensor package sensitive to hydrothermal tracers both persistent and ephemeral, from sources both particle rich and particle poor, to show that the present vent field inventory along fast- to intermediate-rate spreading ridges may underestimate the true value by at least a factor of 3–6.

2. Methods and geological settings

2.1. Sensor characteristics

Our surveys employed sensors that respond to both broadly dispersing (light backscattering, measured as Nephelometric Turbidity Units (NTU)) and ephemeral (oxidation-reduction potential (ORP)) tracers. NTU detects particle-rich discharge, generally at temperatures >~100°C, with copious "black smoker" minerals that create plumes extending tens of kilometers from their source. ORP detects hydrothermal discharge of all temperatures, including low-temperature diffuse venting as well as higher-temperature but particle-poor sources. It responds immediately, with decreasing potential values (*E* (mV)), to the presence of nanomolar concentrations of reduced hydrothermal chemicals (e.g., Fe^{2+}, HS^-, H_2) that are out of equilibrium with the oxidizing ocean (Fig. 1) (Walker et al., 2007; S.L. Walker et al., in preparation). These chemicals rapidly oxidize or metabolize in close proximity to their seafloor source. In this paper, an ORP anomaly is identified by d*E*/dt more negative than -0.04 mV/s for consecutive measurements with an overall decrease (d*E*) >2 mV (e.g., Fig. 2b). This method differentiates anomalies from slowly changing ORP values caused by gradually drifting electrode potentials (either positive or negative) responding to changes in pressure, temperature, or electrode recovery following contact with reduced chemicals. The timescale for redox equilibration of plume fluids is not well constrained, but ORP anomalies caused by Fe^{+2} are expected to dissipate via oxidation to Fe^{+3} within a day (Stranne et al., 2010).

ORP signals thus provide a uniquely high-resolution measurement of discharge-site distribution that discriminates among closely spaced sources. NTU-only anomalies represent sites too distant from our water column observations to produce confirmed ORP anomalies. Based on the length (mean, 0.57±0.72 km; median, 0.30 km) of 290 distinct ORP plume anomalies (>2 mV) (not site separation distance) observed during tows in our four sampling areas, we report a minimum site spacing resolution of 1 km (Figs. 2 and 3). We therefore count NTU or ORP anomalies closer than 1 km as a single discharge site. This precision is comparable to that achieved by autonomous underwater vehicles using tightly gridded surveys to map ORP anomalies found in non-buoyant plumes (German et al., 2008). Because visual seafloor surveys have shown that seafloor vents may be spaced closer than 1 km (e.g., Haymon et al., 1991; Haymon and White, 2004), the abundance and spacing of detected NTU and ORP sites reported here represent minimum values of true vent field abundance and spacing.

To test the validity of the existing view of hydrothermal site spacing, we towed NTU and ORP sensors during four lengthy (100–420 km) and spatially continuous surveys along a cumulative ridge length of 1470 km (~2.2% of total OSR length). We collected data every 5 s (~2–4 m along track) on each tow. Our four study areas include sections spreading at ~50–110 mm/yr and are, therefore, representative of intermediate- to fast-spreading ridges. To make direct comparisons between these data and the existing "common knowledge," we calculated vent site frequency for each ridge section using information from the InterRidge database (Beaulieu et al., 2013, 2015).

2.2. Survey areas

The northern East Pacific Rise (nEPR), 9°–10°N, is a fast-spreading (~100 mm/yr), second-order segment with an axial melt lens (AML) underlying nearly the entire survey area (Carbotte et al., 2013). The nEPR is among the most studied of the global OSR system, yet the only previous continuous survey of hydrothermal plume distribution was conducted in 1991 (Baker et al., 1994). We surveyed the segment from 9.06°–10.03°N (~110 km) in 2011 with NTU/ORP sensor packages attached to the JASON remotely operated vehicle (ROV) at nominal altitudes of 45 m and 60 m above bottom (Fig. 4). Seafloor eruptions occurred in 1991 (prior to the 1991 plume survey) and again in 2005 in approximately the same area (~9.75°–9.93°N), strongly affecting the distribution of venting in that area.

The 420-km-long Eastern Lau Spreading Center (ELSC) is a back-arc ridge with a remarkably high spreading-rate gradient, ranging from 50±10 mm/yr on the Valu Fa Ridge (23°–21.4°S), to 68±7 mm/yr on the central ELSC (21.4°–20.5°S), to 83±9 mm/yr on the northern ELSC (20.5°–19.3°S) (Zellmer and Taylor, 2001). A 1999 seismic survey (Jacobs et al., 2007) found that the Valu Fa Ridge and central ELSC segments showed an almost continuous AML, whereas only a small, isolated melt lens was detected on the faster-spreading northern ELSC segment (Fig. 5). Multiple plume surveys have been conducted on the ELSC (Martinez et al., 2006; Baker et al., 2010). Here we use the most areally complete surveys, which in 2004 collected data from 19.3°–22.8°S along two parallel track lines, nominally ~600 m apart, using an ORP sensor on a tow package ~120 m above bottom and NTU sensors arrayed along the towline.

We mapped hydrothermal plumes along the intermediate-rate (~60 mm/yr) Galápagos Spreading Center (GSC) during two separate expeditions. In 2005 (Baker et al., 2008; Haymon et al., 2008), we used the same sensor array and horizontal tow pattern as for the ELSC along two parallel track lines (~1–2 km offset) between 94.9° and 91.05°W, and along a single track between 90.6° and 89.6°W (Fig. 6). Only the section west of 91.05°W has been seismically surveyed, finding a quasi-continuous AML between ~91.3° and 94.4°W (Detrick et al., 2002). In 2011, we used ORP and NTU sensors on a towed instrument package continuously cycled (wavelength ~750 m) between ~300 m and 20 m above bottom to survey the eastern GSC between 89.4° and 85.8°W (Shank et al., 2012) (Fig. 7).

3. Results

The combined distribution of ORP and NTU anomalies on each ridge section quantitatively locates sites that can then be compared to the distribution of vent sites listed in the authoritative InterRidge database. Because anomalies with a spatial scale as small as ~1 km cannot be precisely illustrated on figures spanning hundreds of kilometers of ridge length, the location of every determined discharge site is tabulated in supplementary material Table S1, noting anomaly type, starting and ending along-track positions defining the site, the resultant path length of each site, and separation between adjacent sites. In this paper we use “diffuse” to mean a site venting low-temperature (<~50°C), particle-poor, low-velocity, disorganized flow; and "discrete" to mean higher-temperature, higher-velocity flow from one or more small orifices. Typically, discrete sites create a plume with abundant particles and a robust optical anomaly.

On the nEPR section, 23 ORP and 24 NTU anomalies identify 27 distinct sites (Fig. 4a,c). The observed site spacing is thus 3.3±2.5 km, one-fourth the 14±7.6 km estimate derived from the InterRidge database. Discharge sites are distributed regularly along the section regardless of the depth of the AML (Fig. 4b). About two-thirds of the ORP anomalies showed coincident temperature anomalies (<0.01°–0.09°C), evidence that JASON commonly intercepted buoyant plumes (e.g., Fig. 2). The substantial along-track length (0.47±0.28 km) of these anomalies suggests that most denote plumes from either extensive diffuse venting, groups of discrete chimneys, or both.

The same analysis on the ELSC yields 175 ORP and 54 NTU anomalies that identify 96 sites (Fig. 5a,c). Mean spacing here is thus 4.2±4.0 km, roughly one-third the 11±8.3 km estimate from the InterRidge database. Mean site separation ranges are 3.7±4.1 km on the slow-spreading Valu Fa Ridge, 5.3±4.9 on the central ELSC, and 4.2±2.9 km on the fast-spreading northern ELSC. Based on a two-tailed *t* test (at the 95% confidence level), the mean site separations do not vary among these segments. Thus, site separation does not vary with AML depth on the Valu Fa Ridge or central ELSC, and remains close even on the northern ELSC where the only detected AML is an isolated event near 20°S (Fig. 5b).

Our observations along these two sections find reductions in vent spacing by factors of 3–4 compared to published estimates. Even this decrease in spacing, however, may underestimate the true disparity between presumed and actual site spacing on other ridges of similar spreading rates because these sections are among the most intensely surveyed in the InterRidge database. In contrast, along two sparsely surveyed sections of the slower-spreading (60 mm/yr) GSC, our revised spacings are 5–6× closer than those calculated from the InterRidge database. On the central GSC, we found 33 ORP and 19 NTU anomalies identifying 33 distinct discharge sites (Fig. 6a,c). Mean site spacing is 13±11 km, compared to 77±73 km based on the InterRidge database. As with the nEPR and ELSC sections, there is no apparent correlation between the distribution of discharge sites and AML presence or depth (Fig. 6b). The scarcity of discharge sites on the central GSC, despite its high magmatic budget, has defied easy explanation. Our detection of widespread ORP-only plumes suggests a crust of high ductility, few deep fractures, and mostly shallow, low-temperature hydrothermal circulation (Baker et al., 2008). Alternatively, time-variant interactions between the GSC and the Galápagos mantle plume may produce temporal episodicity in high-temperature hydrothermal output (Haymon et al., 2008). Results were similar on the eastern GSC, where we found 38 ORP and 14 NTU anomalies identifying 28 distinct discharge sites (Fig. 7a,b). Mean site spacing is 19±25 km, compared to 87±85 km based on the InterRidge database. Combined results from both GSC sections show that 38% of all detected plumes were ORP-only. No seismic surveys to detect an AML distribution have been conducted on the eastern GSC.

Three factors account for the substantial increase in the detection of active discharge sites on these four ridge sections, compared to these and other ridge sections in the InterRidge database. First, detailed exploration requires continuous tows, but that method is seldom used. Towed-sensor surveys account for <20% of OSR sites in the InterRidge database. Second, isolated ORP-only sites are surprisingly common, making up one-quarter of our enumerated sites. These sites likely vent only low-temperature fluids (although we cannot disregard the possibility of some higher-temperature but particle-poor sources), making them difficult to detect with optical sensors or low-resolution chemical sampling. Good examples include vents near 86.3°W on the GSC (Fig. 7) and south of ~22.3°S on the ELSC (Figs. 3 and 5). Third, extensive optical plumes often include discharge from multiple vent fields. High-resolution ORP data allow discrimination of sites spaced as close as ~1 km. A dramatic example is the continuous optical plume between 88.1° and 88.6°W on the GSC, where ORP anomalies reveal three distinct sites (Fig. 7).

We find support for our results in extensive and thorough seafloor visual surveys, including those along the 9°–10°N nEPR ridge section (Fig. 4d). Between 9.15° and 9.9°N, indications of active discharge were observed on camera tows in 38 of 90 intervals of 0.0083° latitude (interval length = 0.93 km, which approximates our 1 km resolution) (Haymon et al., 1991; Haymon and White, 2004). These observations lead to a mean discharge spacing of 2.1±3.0 km, even smaller than our estimate of 3.7±2.5 km (a two-tailed *t* test shows them statistically different at the 95% confidence level). Although the actual site distribution varies somewhat between the 1991 and 2011 data, the important point is that the site frequency and mean separation have changed little over the 20 years between surveys.

On the southern EPR (sEPR) between 17.25° and 18.67°S (spreading rate = 150 mm/yr), abundant optical plume anomalies have been mapped but no ORP data are available (Urabe et al., 1995). Visual inventories here (O’Neill, 1998; Haymon and White, 2004) identified active discharge in 56 of 162 intervals of 0.0083° latitude (0.95 km), for a spacing of 2.8±3.0 km (Fig. 4e). In both the sEPR and nEPR areas, ~50% of the bins had biological communities or diffuse flow but no observed high-temperature vents, an even higher proportion of low-temperature-only venting than our observations of 25% ORP-only vent sites on our four ridge sections. These differences further indicate that our data represent a minimum estimate for the population of active discharge sites.

These results raise an important question. If ORP-only sites represent low-temperature diffuse flow, can plume observations at 50–120 m above bottom detect the majority of such sites? Observations and modeling efforts suggest they can. Plume observations at the eastern end of the eastern GSC section show abundant ORP anomalies in the lowermost 100 m of the water column, whereas NTU anomalies are mostly absent or negligible (Fig. 7). Extensive ROV work during the same expedition found no evidence of high-temperature vents (Shank et al., 2012). On the ELSC, ORP sensors towed through the lowermost 200 m on later site surveys (Baker et al., 2010) found instances of strong ORP anomalies without accompanying NTU anomalies (Fig. 3). Similarly, Haase et al. (2009) found Mn, CH_4, and H_2 anomalies in the lowermost 100–150 m of the water column above the Lilliput vent field (9.5°S, Mid-Atlantic Ridge). Neither high-temperature vents nor plume indications of such venting have been observed around that vent field, despite extensive ROV and water column observations.

Results from a turbulent convection model (Lavelle et al., 2013) indicate that plumes from even small diffuse sources can rise 100 to >200 m. We first modeled a diffuse source of 40 MW, covering a 5 × 5 m area, as observed by Ramondenc et al. (2006) near 9.5°N on the nEPR, and found a plume rise of >200 m (Fig. 8a). This rise height matches our observations for an ORP-only plume on the ELSC (Fig. 3, site 1). We next used a more conservative source of 10 MW spread over a 20 × 20 m area (Fig. 8b). This example corresponds to results from the Lucky Strike vent field (37°N, Mid-Atlantic Ridge), where extensive seafloor observations have measured diffuse heat fluxes ranging from ~6–140 MW, normalized to our modeled 400 m^2 size

(Barreyre et al., 2012). As expected, these conditions reduced the plume rise to ~110 m, still high enough to be detected by our tows at ELSC and GSC.

4. Discussion

To compare our results with published global vent distributions, we use values from 27 ridge sections (Beaulieu et al., 2015) totaling ~15,000 km, or ~20% of the global ridge system (Fig. 9). Vent field spacing is highly variable for slow- and intermediate-rate spreading ridges, decreasing to ~20 km for fast-spreading ridges. For spreading rates >55 mm/yr (14 ridge sections), the reported spacings range from 12–220 km, far wider than our range of 3.3–19 km for the same rate interval. Improved spacing estimates allow, for the first time, quantitative comparisons between observed site distributions and models of hydrothermal processes—such as faunal distributions, geochemical budgets, and crustal fluid circulation—where the number and location of sites are key variables.

4.1. Constraints on faunal distributions

Greater spatial frequency of diffuse venting has profound implications for models of diversity and connectivity of vent faunal communities. For vent animals that exchange recruits by dispersing larvae, and for small-range motile adults, the likelihood of encountering suitable habitat by a dispersal kernel increases with closer site spacing. Models using a 4–5 week pelagic larval life predict optimal success in ridge-crest settlement when dispersal distance ranges between 40 and 100 km (McGillicuddy et al., 2010). With the same larval duration and regional current models, Mitarai et al. (2016) develop connectivity probability pathways for known back-arc vent sites in the western Pacific that demonstrate a high biological isolation. Along the ELSC, strong south-to-north connection probabilities should now increase with our observations of reduced spacing between vents. An area for further tests of frequency/connectivity is in the Mariana back-arc ridge where the model yields a low probability of north/south connections based on known sites.

Equally important is the suitability of habitats for recruiting larvae (Marcus et al., 2009). Our discovery that ORP-only sites are common implies that species persistence is more likely than under the assumption of only widely spaced sites of combined high- and low-temperature venting. Scant data exist on vent larval durations (Hilário et al., 2015), and it is likely that many species have short-lived (<two weeks) larvae with greater on-axis and near-source retention than those currently modeled. For these species, closer vent spacing provides higher survival probabilities and supports the stepping-stone model of connectivity along ridges (Vrijenhoek, 2010). Thus, higher gene flow will reduce genetic drift and diminish speciation events at the terminus of a range. It is the presence of large geographic barriers between venting regions that promotes differentiation (Vrijenhoek, 2010).

A practical application of better knowledge about larval distribution pathways and habitat availability is improved design of deep-sea marine reserves, especially in the context of the environmental management of vent deposit mining (Boschen et al., 2013). While mine sites could be recolonized from nearby low-temperature sites, the high-probability of severe and extensive habitat alteration will demand alternative management tools. Reserve areas selected to represent communities at a mine site, for example, would enhance sustainability (Van Dover et al., 2012; Wedding et al., 2015). Local area networks of low-temperature sites, which would produce the ORP-only plumes we have detected, will provide greater resilience to the chosen reserve through a strong connectivity (Kininmonth et al., 2011) that maintains regional diversity. Because miners target inactive sulphide structures, it is sobering to consider how many of our newly detected sites are minimally active sulphide deposits where mining could instigate faunal eradication—including of deep-sea corals.

Spreading rate reflects the long-term supply of magma to a ridge crest and, therefore, likely influences species diversity through several mechanisms related to vent frequency, stability, and habitat diversity (Juniper and Tunnicliffe, 1997). In archipelago systems (such as ridge segments), the greater abundance of isolated habitats promotes diversity both among and within those habitats by virtue of both the number and overall area of habitats (Cabral et al., 2014). Thus, faster-spreading ridges with denser site spacing and higher variability of habitats should support greater diversity and connectivity. Global comparisons among biogeographic provinces have demonstrated both a relatively greater diversity and site similarity on the EPR (e.g., Moalic et al., 2012), consistent with closely spaced discharge sites. At some point, however, the high disturbance frequency caused by episodic magma supply on superfast ridges may diminish diversity (Juniper and Tunnicliffe, 1997).

In the subseafloor biosphere, high diversity is inferred from analyses of microbial communities in vent fluids (Anderson et al., 2015). Because sustained diffuse venting at individual sites likely fosters local adaptations that underlie these patterns (Opatkiewicz et al., 2009), a seafloor distribution with more sites and a broader range of environmental variability will promote diversification of novel microbial genomes.

4.2. Constraints on geochemical budgets

Although diffuse flow accounts for as much as 90% of axial heat loss (Elderfield and Schultz, 1996), accompanying chemical analyses of the venting fluids are scarce (Bemis et al., 2012). Tantalizingly, studies find that the flux of bioactive chemicals from diffuse flow can exceed that of adjacent high-temperature vents (Wankel et al., 2011), and that diffuse fluids can be rich in organic ligands capable of stabilizing hydrothermal metals in the dissolved state (Sander et al., 2007). Thus, compared to high-temperature vents, a greater percentage of Fe from diffuse flow is available for dispersal throughout the ocean (Toner et al., 2009). This inference is supported by recent modeling efforts (German et al., 2015) showing that diffuse fluids entrained into high-temperature discharge could provide a majority of the hydrothermal Fe supplied to the deep ocean. Fe from isolated sites, such as those feeding the ORP-only plumes described here, was unconsidered in this analysis, as little is known about such sites. If in fact such sites prove to be the kind of diffuse flow envisioned in German et al. (2015), then hydrothermal Fe from diffuse discharge may play a larger role in global biogeochemical budgets than currently presumed (Toner et al., 2009; Resing et al., 2015).

4.3. Constraints on crustal fluid circulation

From a geophysical perspective, our high-resolution, segment-scale discharge data place two specific constraints on models of crustal circulation: isolated ORP-only discharge sites are common, and mean site separation can be small. Isolated ORP-only venting has been little studied, because most seafloor exploration concentrates near high-temperature vents. This sampling bias has supported the presumption that low-temperature discharge predominantly occurs in association with high-temperature vents (Bemis et al., 2012). Our detection of many ORP-only sites implies instead that isolated diffuse venting (and perhaps particle-poor discrete venting) is not uncommon. This view is bolstered by seafloor observations (Haymon et al., 1991; O'Neill, 1998; Haymon and White, 2004; Devey et al., 2010; Larson et al., 2015) and models (Lowell et al., 2003) that describe conditions favorable for isolated diffuse discharge. These include extensive mixing between seawater and upwelling hydrothermal fluids within a porous erupted volcanic layer or along near-axis faults, systems evolving from low- to high-temperature discharge (or vice versa), and hydrothermal circulation hosted in non-basaltic rock.

Site separation distances on our fastest-spreading section, the nEPR (100 mm/yr), yield a modal separation of 2 km (mean = 3.3±2.5 km) (Fig. 10), in qualitative agreement with the close spacing (~1 km) generated in a high-resolution, three-dimensional circulation model for fast-spreading ridges (Hasenclever et al., 2014). Moreover, all four sections have separation modes <5 km (though the eastern GSC also has a higher mode near 17 km). While our results compare more favorably with the model results than does the minimum mean spacing of ~12 km for fast-spreading ridges calculated from the InterRidge database (Fig. 9), we advise caution in transferring these model results to the real world, as the model assumes uniform permeability along axis and a constant heat flux. Geological complications, including structural variations and punctuated heat sources, remain unaddressed. Real-world variations unquestionably contribute to the irregularity in site distributions apparent in our detailed surveys.

One of these irregularities is the remarkable observation that the frequency of discharge sites on the northern ELSC is similar to the rest of the ELSC (and little different from the nEPR) despite the apparent absence of an AML throughout almost the entire segment (Fig. 5).

Discharge sites in this area are evidently powered by a deeper magmatic system without a shallow melt lens (Dunn et al., 2013).

4.4. Implications for other areas

Notable remaining gaps in our understanding of vent site distribution are slow-spreading ridges (<55 mm/yr), which account for half the global ridge length, and the vast and largely unexplored flanks of all ridges, where heat flow studies indicate that 70–90% of oceanic hydrothermal heat loss occurs (Johnson and Pruis, 2003). Although the spatial density of hydrothermal plumes and individual sites (from the InterRidge database) is linearly correlated with spreading rate (and thus the magmatic budget), accumulating evidence suggests that discharge sites are more abundant on slow- and, especially, ultraslow-spreading ridges than predicted by the global trend (Baker and German, 2004; Beaulieu et al., 2015; German et al., 2016). This anomaly implies that non-magmatic heat sources, such as cooling lithospheric rocks and serpentinization, must be common on slow ridges.

Recent summaries of hydrothermal activity on slow ridges (primarily the Mid-Atlantic Ridge) (e.g., Escartin et al., 2008; Rona et al., 2010) support this conclusion. These studies describe a continuum of venting along detachment faults, ranging from high-temperature vents powered by magma beneath axial volcanic ridges, to off-axis high-temperature vents driven by cooling gabbroic intrusions, to distant low-temperature (and occasional high-temperature) vents mining heat from both gabbroic cooling and serpentinization. Venting on the walls and flanks of slow ridges has also been documented outside the Atlantic, such as on the Central Indian Ridge (Son et al., 2014).

Unlike the readily detected sites in neovolcanic zones, sites on axial valley walls and flanks are more resistant to discovery. Low-temperature sites can produce discharge invisible to optical sensors (e.g., Lost City; Larson et al., 2015), but the high concentrations of H_2 in fluids hosted in ultramafic rocks make ORP sensors ideally suited for detecting such plumes. More daunting is the immense lateral scale of slow-spreading ridges. This challenge calls for exploration strategies beyond surface ships, such as the development of efficient, economical, and self-guided autonomous underwater vehicles, coupled with a suite of quick-response sensors for tracers such as CH_4, HS^-, H_2S, Fe, Mn, and others.

5. Conclusions

Decades of surveying along ocean spreading ridges, largely limited to discontinuous measurements of conservative and quasi-conservative tracers, has fostered a “common knowledge” that under-represents the true prevalence of hydrothermal discharge sites. Existing data lead to the conclusion that the mean spacing of active discharge sites on 14 sections of fast- and intermediate-rate spreading ridges ranges from 12–220 km. Our surveys tested this conclusion by towing optical and oxidation-reduction-potential sensors along four ridge sections totaling 1470 km in length. We found discharge site frequency to be 3–6 times greater than that calculated from the authoritative InterRidge database. These higher frequencies lead to site spacings of 3.3–19 km, significantly closer than the 11–87 km spacing determined by using the database. Thus, the inventory of sites on fast- and intermediate-rate ridges may be substantially greater than present estimates, even higher than we report, since our study does not count individual vents with spacings <1 km.

Three factors account for this substantial increase in detected active discharge sites, compared to data in the InterRidge database. First, acquiring continuous plume data greatly increased the likelihood of detecting discharge sites. Second, identifying isolated ORP-only sites, likely venting only low-temperature fluids with a negligible optical signature, increased our enumerated site totals by 25%. Third, closely spaced sites undifferentiated by extensive optical plumes were resolved at a spatial resolution of ~1 km by ORP detection of ephemeral hydrothermal chemicals such as Fe^{2+}, HS^-, and H_2.

We hypothesize that the spacing of active discharge sites on slow-spreading ridges has been similarly underestimated. The variety of heat sources on slow ridges (magma, cooling crustal or mantle rocks, and serpentinization) may create surprising distributions of active venting in axial valleys and on ridge flanks. Further discoveries may thus complicate the present concept of a simple relationship between the frequency of discharge sites and spreading rate. Nonetheless, we possess already the necessary tools to obtain a quantitative measure of global hydrothermal activity.

Acknowledgements

We thank A. Fisher for comments on the manuscript. Three anonymous reviewers likewise provided valuable improvements. This research was supported by the NOAA/PMEL Earth-Ocean Interactions Program and the Joint Institute for the Study of the Atmosphere and Ocean (JISAO) under NOAA Cooperative Agreement No. NA10OAR4320148. PMEL contribution 4379, JISAO contribution 2464.

References

Anderson, R.E., Sogin, M.L., Baross, J.A., 2015. Biogeography and ecology of the rare and abundant microbial lineages in deep-sea hydrothermal vents. FEMS Microbiol. Ecol. 91 (1), doi:10.1093/femsec/fiu016.

Auzende, J.-M., Ballu, V., Batiza, R., Bideau, D., Charlou, J.-L., Cormier, M.H., Fouquet, Y., Geistdoerfer, P., Lagabrielle, Y., Sinton, J., Spadea, P., 1996. Recent tectonic, magmatic, and hydrothermal activity on the East Pacific Rise between 17°S and 19°S: Submersible observations. J. Geophys. Res. 101, 17,995–18,010.

Baker, E.T., German, C.R., 2004. On the global distribution of hydrothermal vent fields. In: German, C.R., Lin, J., Parson, L.M. (Eds.), Mid-Ocean Ridges: Hydrothermal Interactions Between the Lithosphere and Oceans, Geophys. Monogr. Ser. Vol. 148. AGU, Washington, D.C., pp. 245–266.

Baker, E.T., Feely, R.A., Mottl, M.J., Sansone, F.J., Wheat, C.G., Resing, J.A., Lupton, J.E., 1994. Hydrothermal plumes along the East Pacific Rise, 8°40' to 11°50'N: Plume distribution and relationship to the apparent magmatic budget. Earth Planet. Sci. Lett. 128, 1–17.

Baker, E.T., Resing, J.A., Walker, S.L., Martinez, F., Taylor, B., Nakamura, K., 2006. Abundant hydrothermal venting along melt-rich and melt-free ridge segments in the Lau back-arc basin. Geophys. Res. Lett. 33, L07308, doi:10.1029/2005GL025283. Baker, E.T., Haymon, R.M., Resing, J.A., White, S.M., Walker, S.L., Macdonald, K.C., Nakamura, K., 2008. High-resolution surveys along the hot spot-affected Galápagos Spreading Center: 1.

Distribution of hydrothermal activity. Geochem. Geophys. Geosyst. 9, Q09003, doi:10.1029/2008GC002028.

Baker, E.T., Martinez, F., Resing, J.A., Walker, S.L., Buck, N.J., Edwards, M.H., 2010. Hydrothermal cooling along the Eastern Lau Spreading Center: No evidence for discharge beyond the neovolcanic zone. Geochem. Geophys. Geosyst. 11, Q08004, doi:10.1029/2010GC003106.

Barreyre, T., Escartín, J., Garcia, R., Cannat, M., Mittelstaedt, E. Prados, R., 2012. Structure, temporal evolution, and heat flux estimates from the Lucky Strike deep-sea hydrothermal field derived from seafloor image mosaics. Geochem. Geophys. Geosyst. 13, Q04007, doi:10.1029/2011GC003990.

Beaulieu, S.E., Baker, E.T., German, C.R., Maffei, A., 2013. An authoritative global database for active submarine hydrothermal vent fields. Geochem. Geophys. Geosyst. 14, 4892–4905, doi:10.1002/2013GC004998.

Beaulieu, S.E., Baker, E.T., German, C.R., 2015. Where are the undiscovered vents on oceanic spreading ridges? Deep-Sea Res. Pt. II 121, 202–212, doi:10.1016/j.dsr2.2015.05.001.

Bemis, K., Lowell, R.P., Farough, A., 2012. Diffuse flow on and around hydrothermal vents at mid-ocean ridges. Oceanography 25, 182–191, doi:10.5670/oceanog.2012.16.

Boschen, R.E., Rowden, A.A., Clark, M.R., Gardner, J.P.A., 2013. Mining of deep-sea seafloor massive sulfides: A review of the deposits, their benthic communities, impacts from mining, regulatory frameworks and management strategies. Ocean Coast. Manage. 84, 54–67, doi:10.1016/j.ocecoaman.2013.07.005.

Cabral, J.S., Weigelt, P., Kissling, W.D., Kreft, H., 2014. Biogeographic, climatic and spatial drivers differentially affect α-, β- and γ-diversities on oceanic archipelagos. Proc. Roy. Soc. B-Bio. Sci. 281, doi:10.1098/rspb.2013.3246.

Carbotte, S.M., Marjanović, M., Carton, H., Mutter, J.C., Canales, J.P., Nedimović, M.R., Han, S., Perfit, M.R., 2013. Fine-scale segmentation of the crustal magma reservoir beneath the East Pacific Rise. Nature Geosci. 6, 866-870, doi:10.1038/ngeo1933.

Detrick, R.S., Sinton, J.M., Ito, G., Canales, J.P., Behn, M., Blacic, T., Cushman, B., Dixon, J.E., Graham, D.W., Mahoney, J.J., 2002. Correlated geophysical, geochemical, and volcanological manifestations of plume-ridge interaction along the Galápagos Spreading Center. Geochem. Geophys. Geosyst. 3, 8501, doi:10.1029/2002GC000350.

Devey, C.W., German, C.R., Haase, K.M., Lackschewitz, K.S., Melchert, B., Connelly, D.P., 2010. The relationships between volcanism, tectonism, and hydrothermal activity on the southern equatorial Mid-Atlantic Ridge. In: Rona, P.A., Devey, C.W., Dyment, J., Murton, B. (Eds.), Diversity of Hydrothermal Systems on Slow Spreading Ocean Ridges, Geophys. Monogr. Ser. Vol. 188. AGU, Washington D.C., pp. 133–152.

Dunn, R.A., Martinez, F., Conder, J.A., 2013. Crustal construction and magma chamber properties along the Eastern Lau Spreading Center. Earth Planet. Sci. Lett., 371, 112-124.

Elderfield, H., Schultz, A., 1996. Mid-ocean ridge hydrothermal fluxes and the chemical composition of the ocean. Annu. Rev. Earth Planet. Sci. 24, 191–224.

Escartin, J., Smith, D.K., Cann, J., Schouten, H., Langmuir, C.H., Escrig, S., 2008. Central role of detachment faults in accretion of slow-spreading oceanic lithosphere. Nature 455, 790–794, doi:10.1038/nature07333.

Fisher, A.T., Becker, K., 2000. Channelized fluid flow in oceanic crust reconciles heat-flow and permeability data. Nature 403, 71–74.

Fouquet, Y., von Stackelberg, U., Charlou, J.L., Donval, J.P., Foucher, J.P., Erzinger, J., Herzig, P., Mühe, R., Wiedicke, M., Soakai, S., Whitechurch, H., 1991. Hydrothermal activity in the Lau back-arc basin: Sulfides and water chemistry. Geology 19, 303–306.

German, C.R., Parson, L.M., 1998. Distributions of hydrothermal activity along the Mid-Atlantic Ridge: Interplay of magmatic and tectonic controls. Earth. Planet. Sci. Lett. 160, 327–341.

German, C.R., Yoerger, D.R., Jakuba, M., Shank, T.M., Langmuir, C.H. and Nakamura, K.I., 2008. Hydrothermal exploration with the autonomous benthic explorer. Deep Sea Res. Part I 55, 203–219.

German, C.R., Legendre, L.L., Sander, S.G., Niquil, N., Luther, G.W., Bharati, L., Han, X., Le Bris, N., 2015. Hydrothermal Fe cycling and deep ocean organic carbon scavenging: Model-based evidence for significant POC supply to seafloor sediments. Earth Planet. Sci. Lett. 419, 143–153, doi:10.1016/j.epsl.2015.03.012.

German, C.R., Petersen, S., Hannington, M.D., 2016. Hydrothermal exploration of mid-ocean ridges: Where might the largest sulfide deposits be forming? Chem. Geol. 420, 114–126, doi:10.1016/j.chemgeo.2015.11.006.

Haase, K.M., Koschinsky, A., Petersen, S., Devey, C.W., German, C., Lackschewitz, K.S., Melchert, B., Seifert, R., Borowski, C., Giere, O., Paulick, H., 2009. Diking, young volcanism and diffuse hydrothermal activity on the southern Mid-Atlantic Ridge: The Lilliput field at 9°33′ S. Mar. Geol. 266, 52–64.

Hannington, M., Jamieson, J., Monecke, T., Petersen, S., Beaulieu, S., 2011. The abundance of seafloor massive sulfide deposits. Geology 39, 1155–1158, doi:10.1130/G32468.1.

Hasenclever, J., Theissen-Krah, S., Rüpke, L.H., Morgan, J.P., Iyer, K., Petersen, S., Devey, C.W., 2014. Hybrid shallow on-axis and deep off-axis hydrothermal circulation at fast-spreading ridges. Nature 508, 508–512, doi:10.1038/nature13174.

Haymon, R.M., White, S.M., 2004. Fine-scale segmentation of volcanic/hydrothermal systems along fast-spreading ridge crests. Earth Planet. Sci. Lett. 226, 367–382.

Haymon, R. M., Fornari, D. J., Edwards, M., Carbotte, S. M., Wright, D., Macdonald, K. C., 1991. Hydrothermal vent distribution along the East Pacific Rise crest (9°09'–9°54' N) and its relationship to magmatic and tectonic processes on fast-spreading mid-ocean ridges. Earth Planet. Sci. Lett. 104, 513–534.

Haymon, R.M., White, S.M., Baker, E.T., Anderson, P.G., Macdonald, K.C., Resing, J.A., 2008. High-resolution surveys along the hot spot-affected Gálapagos Spreading Center: 3. Black smoker discoveries and the implications for geological controls on hydrothermal activity. Geochem. Geophys. Geosyst. 9, Q12006, doi:10.1029/2008GC002114.

Hilário, A., Metaxas, A., Gaudron, S.M., Howell, K.L., Mercier, A., Mestre, N.C., Ross, R.E., Thurnherr, A.M., Young, C., 2015. Estimating dispersal distance in the deep sea: Challenges and applications to marine reserves. Frontiers Mar. Sci. 2, 6, doi:10.3389/fmars.2015.00006.

Jacobs, A.M., Harding, A.J., Kent, G.M., 2007. Axial crustal structure of the Lau back-arc basin from velocity modeling of multichannel seismic data. Earth Planet. Sci. Lett. 259, 239–255, doi:10.1016/j.epsl.2007.04.021.

Johnson, H.P., Pruis, M.J., 2003. Fluxes of fluid and heat from the oceanic crustal reservoir. Earth Planet. Sci. Lett. 216, 565–574.

Juniper, S.K., Tunnicliffe, V., 1997. Crustal accretion and the hot vent ecosystem. Philos. T. Roy. Soc. A. 355, 459-474.

Kininmonth, S., Beger, M., Bode, M., Peterson, E., Adams, V.M., Dorfman, D., Brumbaugh, D.R., Possingham, H.P., 2011. Dispersal connectivity and reserve selection for marine conservation. Ecol. Model. 222, 1272–1282.

Larson, B.I., Lang, S.Q., Lilley, M.D., Olson, E.J., Lupton, J.E., Nakamura, K., Buck, N.J., 2015. Stealth export of hydrogen and methane from a low temperature serpentinization system. Deep-Sea Res. Part II 121, 233–245.

Lavelle, J.W., Di Iorio, D., Rona, P., 2013. A turbulent convection model with an observational context for a deep-sea hydrothermal plume in a time-variable cross flow. J. Geophys. Res. 118, 6145–6160, doi:10.1002/2013JC009165.

Lowell, R.P., Yao, Y., Germanovich, L.N., 2003. Anhydrite precipitation and the relationship between focused and diffuse flow in seafloor hydrothermal systems. J. Geophys. Res. 108, 2424, doi:10.1029/2002JB002371.

Marcus, J., Tunnicliffe, V., Butterfield, D.A., 2009. Post-eruption succession of macrofaunal communities at diffuse flow hydrothermal vents on Axial Volcano, Juan de Fuca Ridge, Northeast Pacific. Deep-Sea Res. Part II 56, 1586–1598, doi:10.1016/j.dsr2.2009.05.004.

Martinez, F., Taylor, B., Baker, E.T., Resing, J.A., Walker, S.L., 2006. Opposing trends in crustal thickness and spreading rate along the back-arc Eastern Lau Spreading Center: Implications for controls on ridge morphology, faulting, and hydrothermal activity. Earth Planet. Sci. Lett. 245, 655–672, doi:10.1016/j.epsl.2006.03.049.

McGillicuddy, D.J., Lavelle, J.W., Thurnherr, A M., Kosnyrev, V.K., Mullineaux, L.S., 2010. Larval dispersion along an axially symmetric mid-ocean ridge. Deep-Sea Res. Part I 57, 880–892, doi:10.1016/j.dsr.2010.04.003.

Mitarai, S., Watanabe, H., Nakajima, Y., Shchepetkin, A.F., McWilliams, J.C., 2016. Quantifying dispersal from hydrothermal vent fields in the western Pacific Ocean. Proc. Nat. Acad. Sci. 113, 2976–2981, doi:10.1073/pnas.1518395113.

Moalic, Y., Desbruyères, D., Duarte, C.M., Rozenfeld, A.F., Bachraty, C., Arnaud-Haond, S., 2012. Biogeography revisited with network theory: Retracing the history of hydrothermal vent communities. Syst. Biol. 61, 127–137, doi:10.1093/sysbio/syr088.

O'Neill, J.H., 1998. Geologic controls on distribution of hydrothermal vents on the superfast-spreading southern East Pacific Rise. Master's Thesis Dissertation, University of California, Santa Barbara, 69 pp.

Opatkiewicz, A.D., Butterfield, D.A., Baross, J.A., 2009. Individual hydrothermal vents at Axial Seamount harbor distinct subseafloor microbial communities. FEMS Microbiol. Ecol. 70, 413–424, doi:10.1111/j.1574-6941.2009.00747.x.

Ramondenc, P., Germanovich, L.N., Von Damm, K.L. and Lowell, R.P., 2006. The first measurements of hydrothermal heat output at 9°50′ N, East Pacific Rise. Earth Planet. Sci. Lett. 245, 487-497.

Resing, J.A., Sedwick, P.N., German, C.R., Jenkins, W.J., Moffett, J.W., Sohst, B.M., Tagliabue, A., 2015. Basin-scale transport of hydrothermal dissolved metals across the South Pacific Ocean. Nature 523, 200–203, doi:10.1038/nature14577.

Rona, P.A., Devey, C.W., Dyment, J., Murton, B.J., 2010. Diversity of Hydrothermal Systems on Slow Spreading Ocean Ridges, Geophys. Monogr. Ser. Vol. 188. AGU, Washington, D.C.

Sander, S.G., Koschinsky, A., Massoth, G., Stott, M., Hunter, K.A., 2007. Organic complexation of copper in deep-sea hydrothermal vent systems. Environ. Chem. 4, 81–89.

Shank, T.M., Baker, E.T., Embley, R.W., Hammond, S., Holden, J.F., White, S., Walker, S.L., Calderon, M., Herrera, S., Lin, T.J., Munro, C., Heyl, T., Stewart, L.C., Malik, M., Lobecker, E., Potter, J., 2012. Exploration of the deepwater Galápagos region. In: Bell, K.L.C., Elliott, K., Martinez, C., Fuller, S.A. (Eds.), New Frontiers in Ocean Exploration: The E/V *Nautilus* and NOAA Ship *Okeanos Explorer* 2011 Field Season. Oceanography 25 (Suppl.), 50–51.

Son, J., Pak, S.-J., Kim, J., Baker, E.T., You, O.-R., Son, S.-K., Moon, J.-W., 2014. Tectonic and magmatic control of hydrothermal activity along the slow-spreading Central Indian Ridge, 8°S–17°S. Geochem. Geophys. Geosyst. 15, 2011–2020, doi:10.1002/2013GC005206.

Stranne, C., Sohn, R.A., Liljebladh, B., Nakamura, K., 2010. Analysis and modeling of hydrothermal plume data acquired from the 85°E segment of the Gakkel Ridge. J. Geophys. Res. 115, C06028, doi:10.1029/2009JC005776.

Toner, B.M., Fakra, S.C., Manganini, S.J., Santelli, C.M., Marcus, M.A., Moffett, J.W., Rouxel, O., German, C.R., Edwards, K.J., 2009. Preservation of iron (II) by carbon-rich matrices in a hydrothermal plume. Nat. Geosci. 2, 197–201, doi:10.1038/ngeo433.

Urabe, T., Baker, E.T., Ishibashi, J., Feely, R.A., Marumo, K., Massoth, G.J., Maruyama, A., Shitashima, K., Okamura, K., Lupton, J.E., Sonada, A., Yamazaki, T., Aoki, M., Gendron, J., Green, R., Kaiho, Y., Kisimoto, K., Lebon, G., Matsumoto, T., Nakamura, K., Nishizawa, A., Okano, O., Paradis, G., Roe, K., Shibata, T., Tennant, D., Vance, T., Walker, S.L., Yabuki, T., Ytow, N., 1995. The effect of magmatic activity on hydrothermal venting along the superfast-spreading East Pacific Rise. Science 269, 1092–1095.

Van Dover, C.L., Smith, C.R., Ardron, J., Dunn, D., Gjerde, K., Levin, L., Smith, S., 2012. Designating networks of chemosynthetic ecosystem reserves in the deep sea. Mar. Policy 36, 378–381.

Vrijenhoek, R.C., 2010. Genetic diversity and connectivity of deep-sea hydrothermal vent metapopulations. Mol. Ecol. 19, 4391–4411, doi:10.1111/j.1365-294X.2010.04789.x.

Walker, S.L., Baker, E.T., Resing, J.A., Nakamura, K., McLain, P.D., 2007. A new tool for detecting hydrothermal plumes: An ORP Sensor for the PMEL MAPR, Eos Trans. AGU 88(52), Fall Meet. Suppl., Abstract V21D-0753.

Wankel, S.D., Germanovich, L.N., Lilley, M.D., Genc, G., DiPerna, C.J., Bradley, A.S., Olson, E.J., Girguis, P.R., 2011. Influence of subsurface biosphere on geochemical fluxes from diffuse hydrothermal fluids. Nat. Geosci. 4, 461–468, doi:10.1038/ngeo1183.

Wedding, L.M., Reiter, S.M., Smith, C.R., Gjerde, K.M., Kittinger, J.N., Friedlander, A.M., Gaines, S.D., Clark, M.R., Thurnherr, A.M., Hardy, S.M., Crowder, L.B., 2015. Managing mining of the deep seabed. Science 349, 144–145.

Zellmer, K.E., Taylor, B., 2001. A three-plate kinematic model for Lau Basin opening. Geochem. Geophys. Geosyst. 2(5), 1020, doi:10.1029/2000GC000106.

Artwork

Figure 1. Laboratory response of multiple ORP sensors in the same bath during a single exposure to (a) Fe^{+2} (dissolved ferrous ammonium sulphate) and (b) sulphide (dissolved NaS) (Walker et al., 2007; S.L. Walker et al., in preparation). All ORP values are the raw (electric) potential reading of an inert Pt electrode against a KCl saturated Ag-AgCl reference electrode. Responses result in an immediate decline in voltage, followed by a lengthy recovery once the reduced chemicals are flushed from the bath; the sulphide cycle is longer than for Fe^{+2}. The recovery cycle does not affect the magnitude of subsequent responses. Values of individual sensors can vary by tens of millivolts, but absolute values are unimportant when using the sensor for only qualitative detection of hydrothermal plumes. Initial concentrations were ~90 nM for Fe^{+2} and ~800 nM for NaS. In-situ calibration is impossible because plumes contain varying mixtures of multiple reduced chemicals.

Figure 2. In-situ responses of an ORP sensor (blue/black lines) being towed horizontally (~60 m above bottom) through an area of multiple vent sources on the East Pacific Rise. (a) We define the path length of an ORP response (black lines) as extending from initial response to maximum decline. Multiple responses within 1 km are considered a single discharge site. In this near-bottom tow, ORP responses were precisely correlated with the occurrence of temperature spikes (red), unequivocal indicators of a hydrothermal plume. ORP responses occur even in the absence of an NTU (green) response, as from particle-poor, low-temperature discharge. (b) High-resolution comparisons of ORP and temperature anomalies, from the same tow, demonstrate that an ORP response as small as 2 mV (at 9.3778°N) is correlated with a temperature spike, and thus

indicative of hydrothermal discharge. In this paper, an ORP anomaly is any measurement decrease ≥2 mV that lasts for at least two measurements, has a rate of decline >0.04 mV/s, and then begins a recovery. Measurements occurred every 5 s on all surveys. Anomalies in both panels likely represent buoyant fluids rising from the seafloor, from either broad diffuse fields and/or groups of discrete vents.

Figure 3. Examples of using ORP and NTU anomalies to identify types of hydrothermal discharge sites. (a) Along-axis plume signals from a tow along the Eastern Lau Spreading Center (Baker et al., 2010) using multiple ORP (top) and NTU (bottom) sensors. To improve clarity in this figure, all ORP sensors were normalized to a value of 375 mV at latitude 22.25°S. ORP and NTU sensors were fastened to the towline at various depths, given in the inset as relative to the depth of the tow vehicle, nominally kept at an altitude of ~110 m above bottom. Locations of observed active sites are numbered; yellow bars indicate confirmed vent sites from the InterRidge database. Note that ORP signals can be detected at altitudes >200 m above bottom (red line) even in the absence of NTU anomalies (site 1). (b) The numbered sites (red triangles), plotted here in relation to the tow path (black line), have distinctive plume signatures: (1) inferred, robust low temperature site with no NTU anomaly; (2,8) confirmed low-temperature sites; (3) distant (no ORP) high-temperature site; (4,5,6,7) nearby high-temperature sites. Site 7 (White Church) (Fouquet et al., 1991) was discovered in 1989 and may be improperly located as off axis. All sites extend <0.5 km along axis.

Figure 4. Indicators of hydrothermal activity along the northern East Pacific Rise. Data collected by single ORP and NTU sensors on a remotely operated vehicle ~60 m above bottom. (a)

Distribution of InterRidge database sites (arrows) and sites determined by this survey (yellow circles). Circles are plotted at the beginning of an ORP or NTU profile signal and thus may be offset from the maximum ORP or NTU value. (b) Depth below the seafloor of the axial magma lens (Carbotte et al., 2013). Gaps in the AML may result from ship wander along the axis. (c) Continuous ORP (red) and NTU (blue) data. Some anomalies are difficult to discern on the profile data because of occasional ROV reversing along the track line. Bottom panels show locations of all ORP and NTU anomalies. (d) Locations of active vents (enumerated vents, red bars) and diffuse flow or vent biology (presence/absence only, cyan bars) from historical camera tows and submersible observations, binned at 0.93 km (0.0083°) intervals (Haymon et al., 1991; Haymon and White, 2004). Following Haymon and White (2004), areas south of 9.45ºN with low (1–4) animal frequencies are not included here. (e) Indicators of hydrothermal activity along the southern East Pacific Rise, 17.2°-18.7°S. Locations of active vents (enumerated vents, red bars) and diffuse flow or vent biology (presence/absence only, cyan bars) from historical camera tows and submersible observations, binned at 0.95 km (0.0083°) intervals (O'Neill, 1998; Haymon et al., 1991; Haymon and White, 2004). Double-headed arrows show areas of the most intensive camera surveys.

Figure 5. Indicators of hydrothermal activity along the Eastern Lau Spreading Center. Data collected along two parallel track lines, nominally ~600 m apart, by an ORP sensor on a tow package ~120 m above bottom and by NTU sensors arrayed along the towline. (a) Distribution of InterRidge database sites (arrows) and sites determined by this survey (yellow circles). Circles are plotted at the beginning of an ORP or NTU profile signal and thus may be offset from the maximum ORP or NTU value. (b) Depth below the seafloor of the axial magma lens (Jacobs et

al., 2007). The isolated AML event at ~20°S has no depth determination. N.D. indicates area of no seismic coverage. (c) Continuous ORP (red and orange) and NTU (blues) data for both track lines. Bottom panels show locations of ORP anomalies from the vehicle-mounted sensor and optical anomalies from all sensors (NTU). (For clarity in these panels, some symbols must be slightly longer than the actual anomaly, and closely spaced anomalies are offset vertically.)

Figure 6. Indicators of hydrothermal activity along the central Galápagos Spreading Center. Data collected along two parallel track lines (~1–2 km offset) by an ORP sensor on a tow package ~120 m above bottom and by NTU sensors above and below the package. (a) Distribution of InterRidge database sites (arrows) and sites determined by this survey (yellow circles). Circles are plotted at the beginning of an ORP or NTU profile signal and thus may be offset from the maximum ORP or NTU value. (b) Depth below the seafloor of the axial magma lens (Detrick et al., 2002). N.D. indicates areas of no seismic coverage. (c) Continuous ORP (red and orange) and NTU (blues) data from each towline. Bottom panels show locations of individual anomalies from the ORP sensor, the vehicle-mounted NTU sensor (NTUv), and all NTU sensors (NTU). (For clarity in these panels, some symbols must be slightly longer than the actual anomaly, and closely spaced anomalies are offset vertically.) Because some anomalies only registered on NTU sensors deeper than the vehicle, some ORP-only sites may have gone undetected.

Figure 7. Indicators of hydrothermal activity along the eastern Galápagos Spreading Center. Data were collected west of 89.6°W in 2006 on a single horizontal tow with an ORP sensor ~120 m above bottom and by NTU sensors arrayed along the towline (as in Fig. 6). Data east of 89.3°W were collected in 2011 by ORP and NTU sensors on a three separate tows with an instrument

package continuously cycled between 300 m and 20 m above bottom. Cycle wavelength ~750 m. (a) Distribution of InterRidge database sites (arrows) and sites determined by this survey (yellow circles). Circles are plotted at the beginning of an ORP or NTU profile signal and thus may be offset from the maximum ORP or NTU value. (b) Continuous ORP (red) and NTU (blue) data. Bottom panels show locations of ORP and NTU anomalies. (For clarity in these panels, some symbols must be slightly longer than the actual anomaly, and closely spaced anomalies are offset vertically.)

Figure 8. Animations of buoyant plumes from diffuse seafloor sources. (a) A diffuse source plume resulting from a thermal discharge of 40 MW over a 5 m × 5 m region as it spreads at 7 hr (model run time) on its level of neutral buoyancy some 200 m or more above its source depth. Ambient conditions include a still flow, stratification with a potential density gradient 5.307×10^5 kg/m^4 (characteristic of the East Pacific Rise at 9°N at depth), and Coriolis parameter of $f = 4.95 \times 10^{-5}$. In this experiment, model resolution was 1.25 m × 1.25 m × 2.5 m × 2 s. (b) A plume at 12 hr with the diffuse source size enlarged to 20 m × 20 m and the thermal flux reduced to 10 MW. Note the differences between panels in spatial and temporal scales. In this reduced heat flux case, the level of neutral buoyancy is 110 m above source, about half that of the example in (a), and temperature anomalies are all smaller too. The larger source area dictated model cell size of 2.5 m × 2.5 m × 2.5 m × 4 s.

Figure 9. Scatter plot of site spacing vs. spreading rate for 27 ridge sections using data from the InterRidge database (red dots). The four sections studied here are symbol-coded: central Galápagos Spreading Center (inverted triangles), eastern Galápagos Spreading Center (upright

triangles), Eastern Lau Spreading Center (diamonds), northern East Pacific Rise (squares), and southern East Pacific Rise (skewed triangles). Site spacing (variability = $\pm 1\sigma$ of mean spacing values) for these sections is color-coded: InterRidge database spacing (large red symbols), spacing calculated in this study (green), and spacing derived from visual seafloor observations only (purple). InterRidge values for the northern and southern East Pacific Rise are for portions of the full sections (red dots) where ORP data and/or seafloor observations are available. Double-headed horizontal arrow for the Eastern Lau Spreading Center indicates the range of spreading rates for that ridge section. Ranges for other sections are smaller than the symbol size.

Figure 10. Histograms of vent site spacing at the four ridge sections discussed in the text, based on ORP and NTU data binned at 1 km intervals. (a) East Pacific Rise, 9°–10°N (mean = 3.3±2.5 km; median = 2.7 km); (b) Eastern Lau Spreading Center (mean = 4.2±4.0 km; median = 3.1 km); (c) central Galápagos Spreading Center (mean = 13±11 km; median = 9.0 km); (d) eastern Galápagos Spreading Center (mean = 19±25 km; median = 14 km). (Note break on the x-axis.)

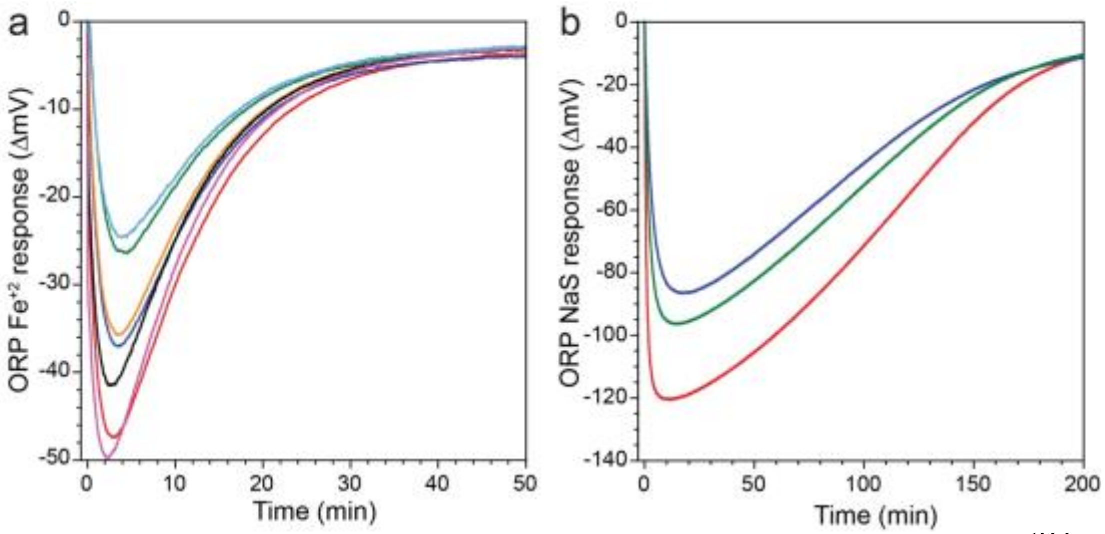

Figure 1

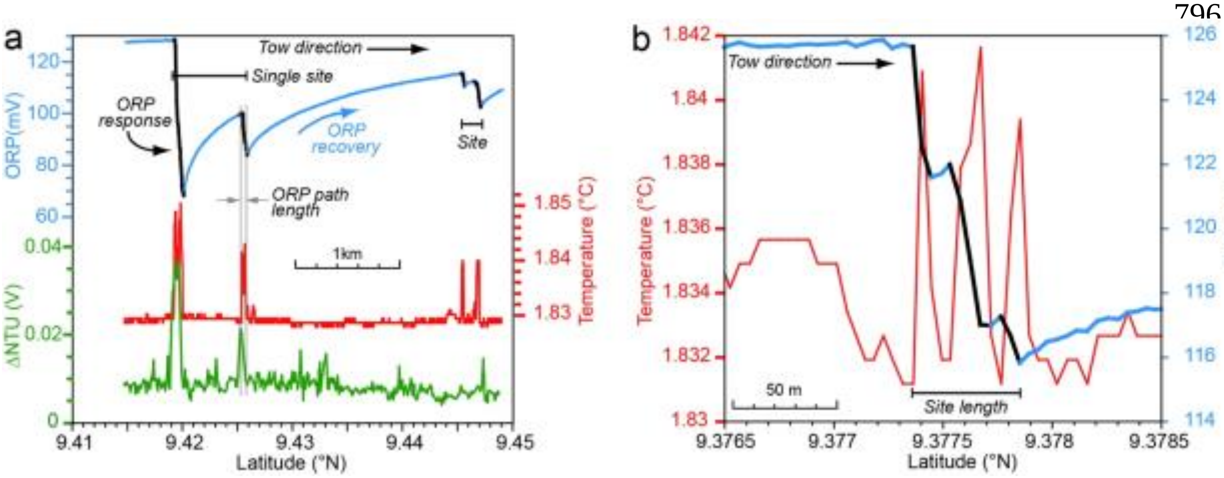

Figure 2igure 3

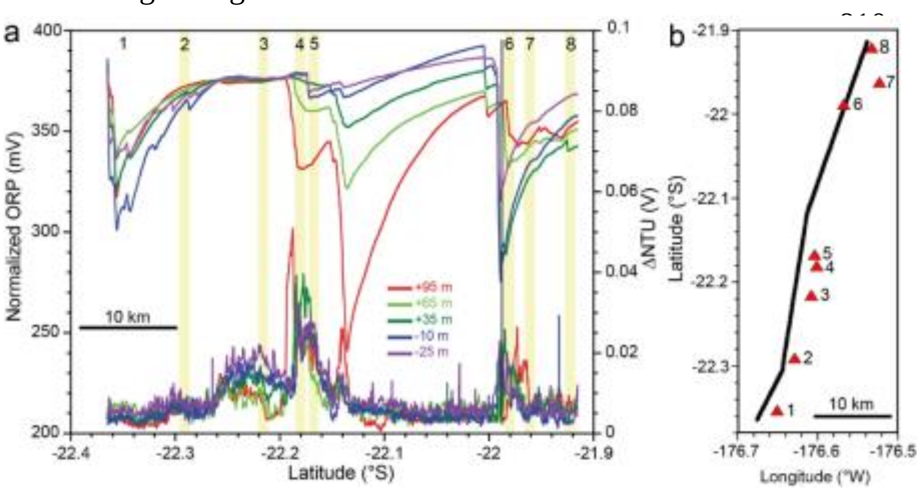

Figure 3

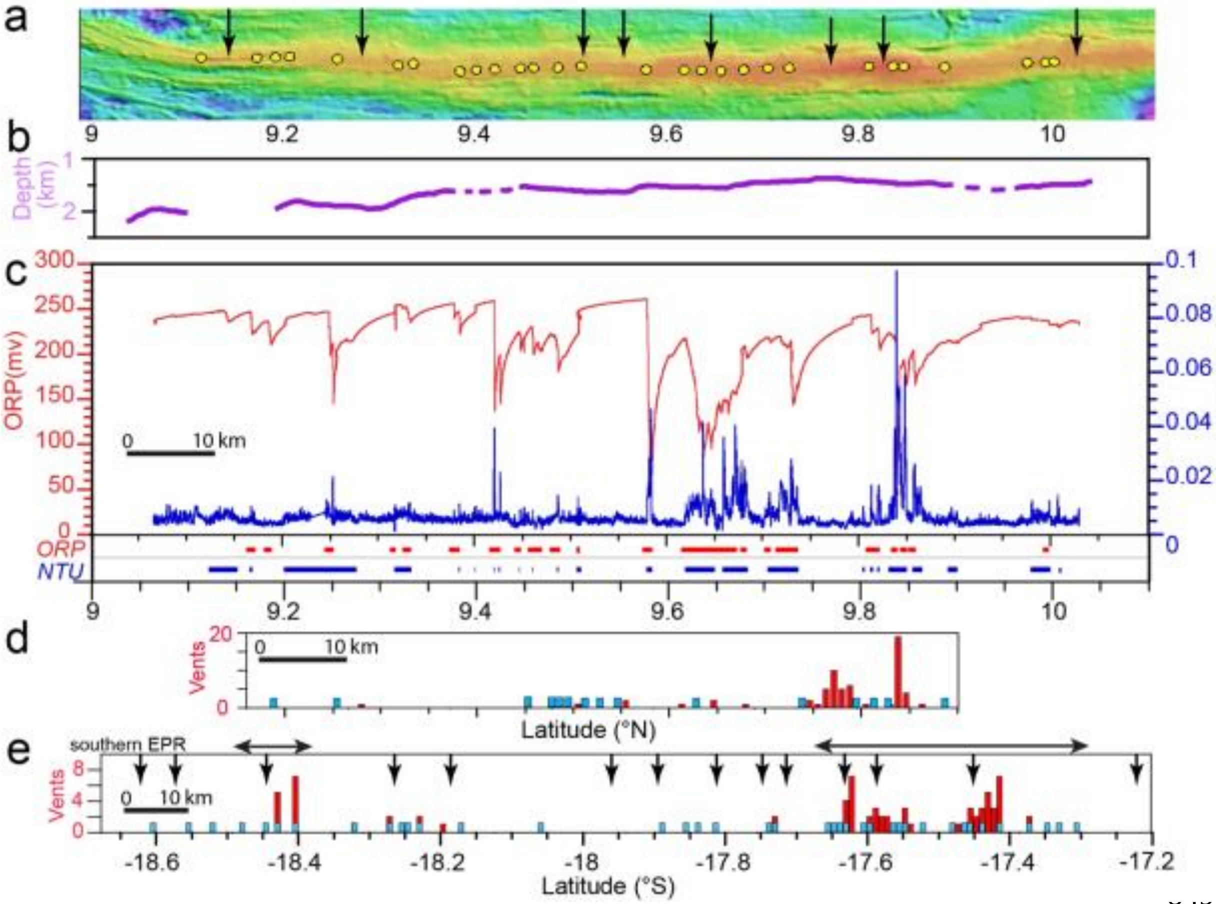

Figure 4

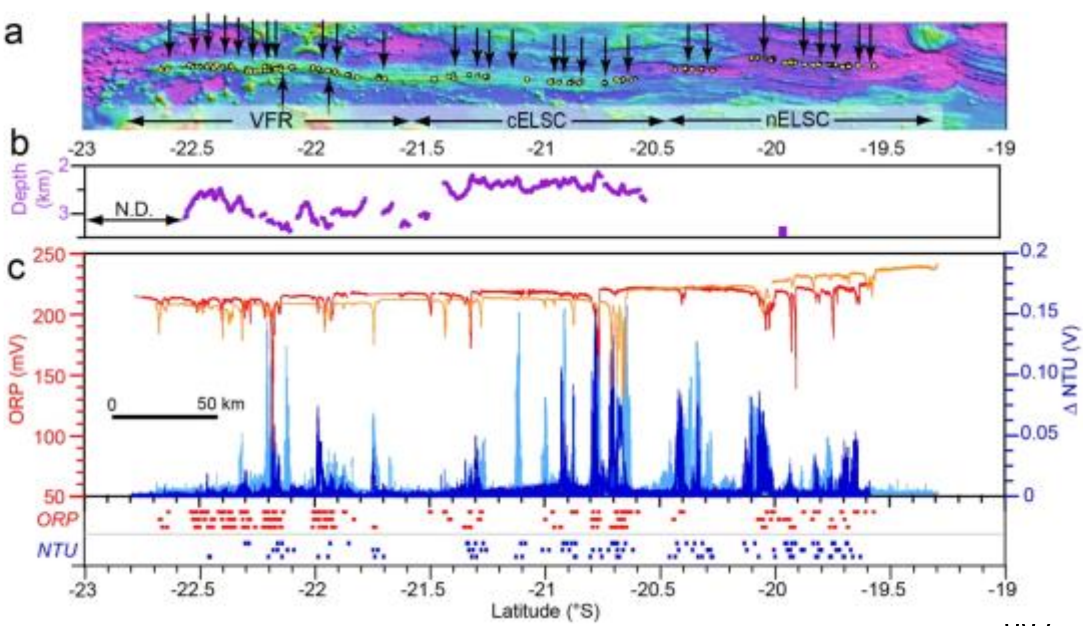

Figure 5

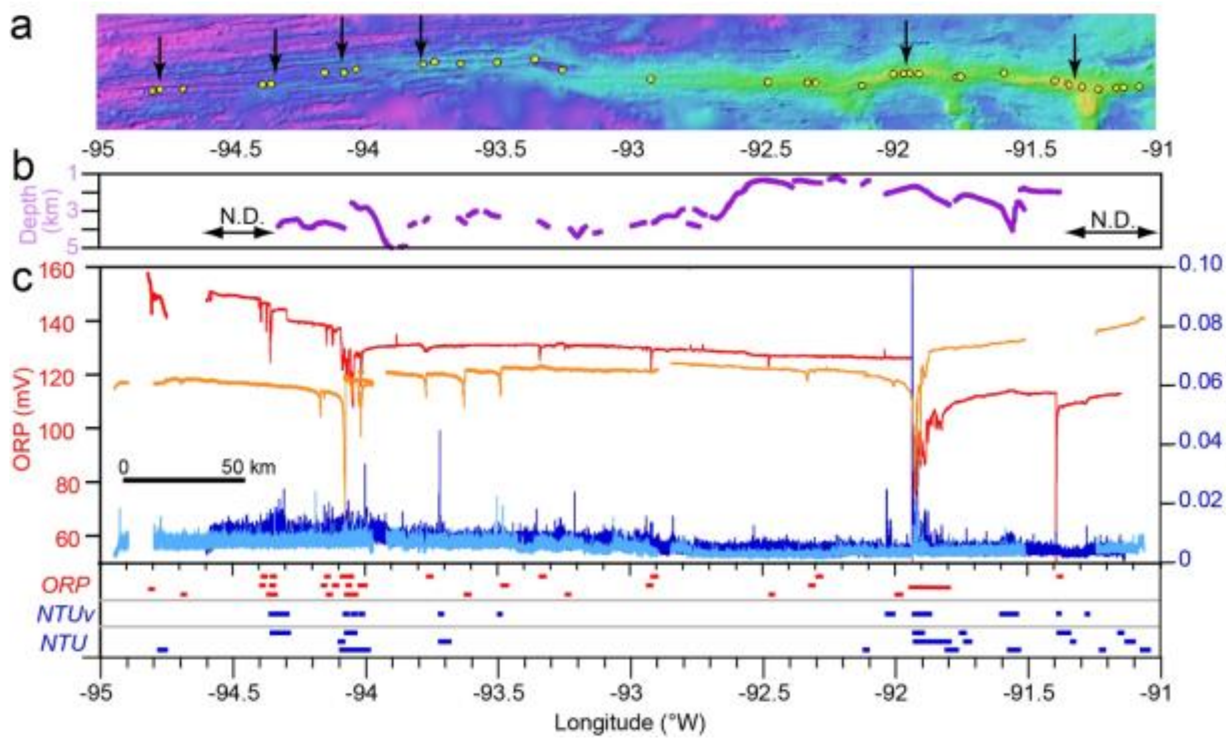

Figure 6

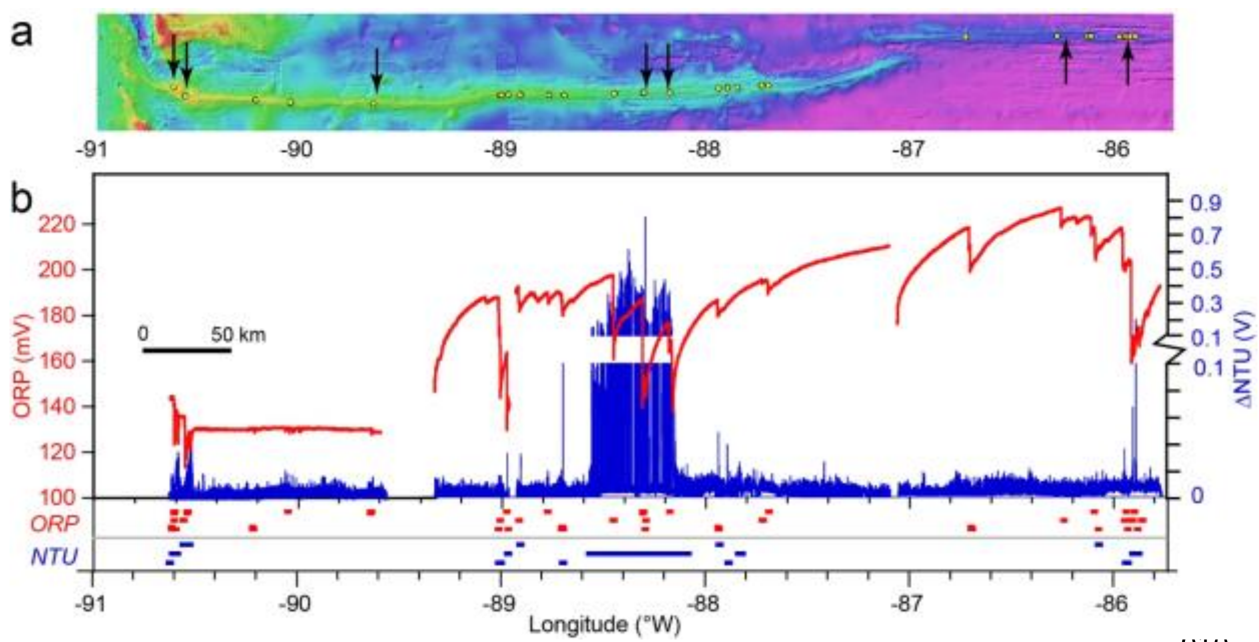

Figure 7

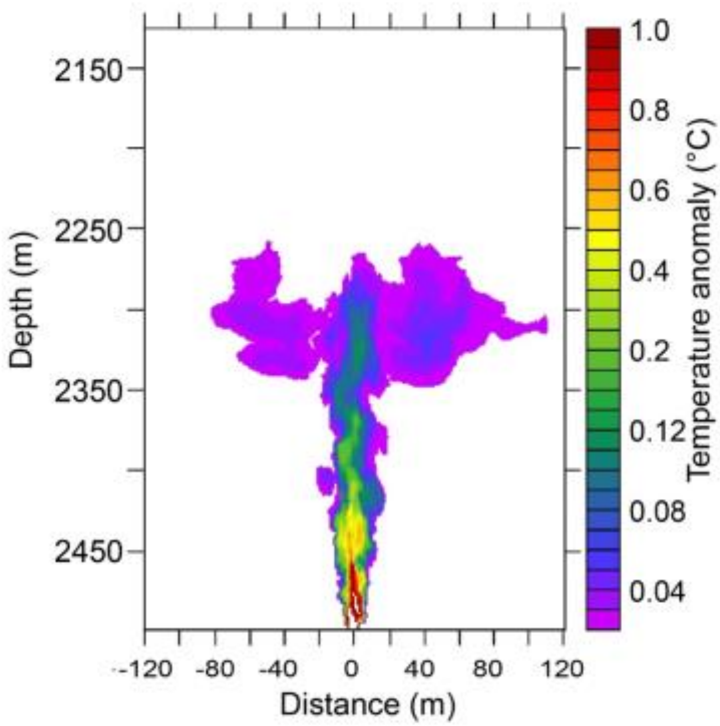

Figure 8A

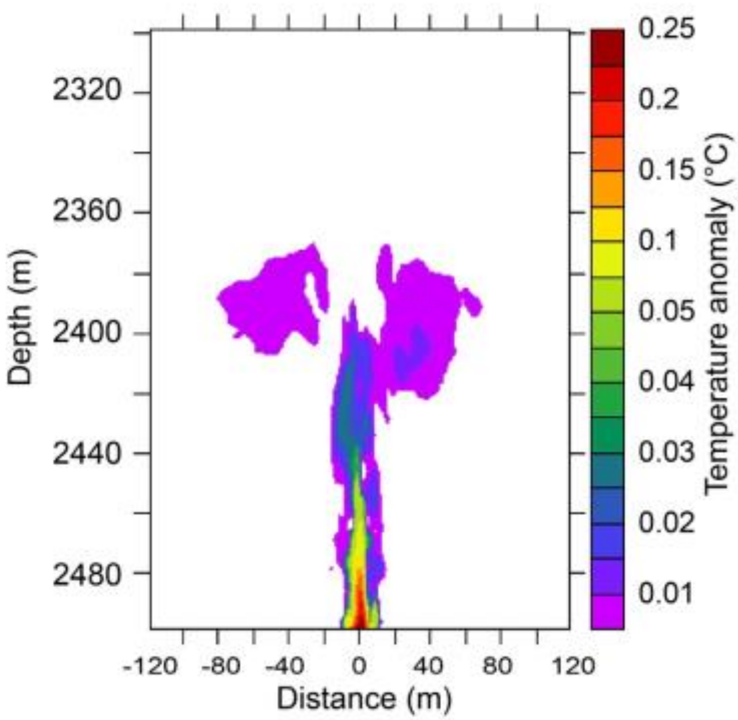

Figure 8B

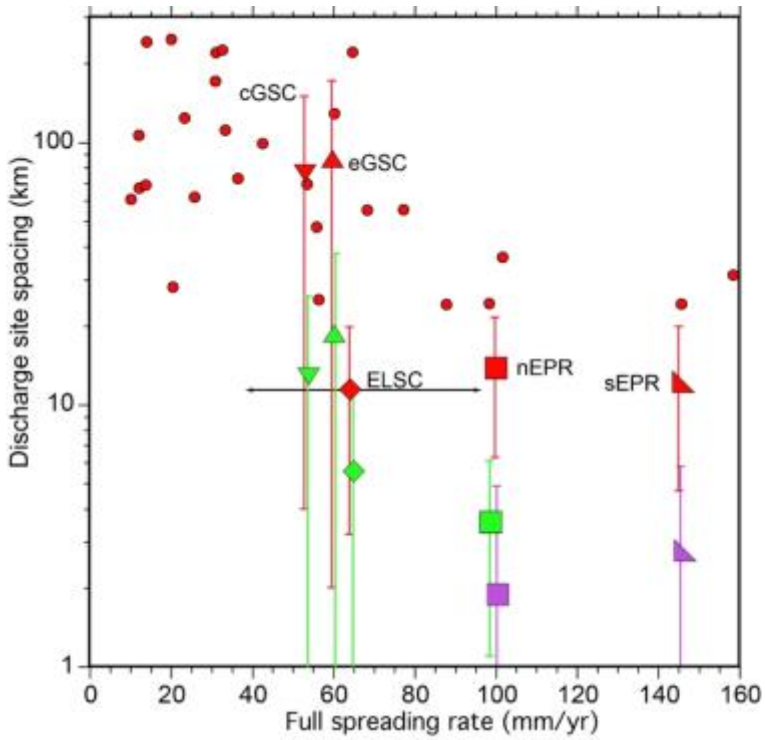

Figure 9

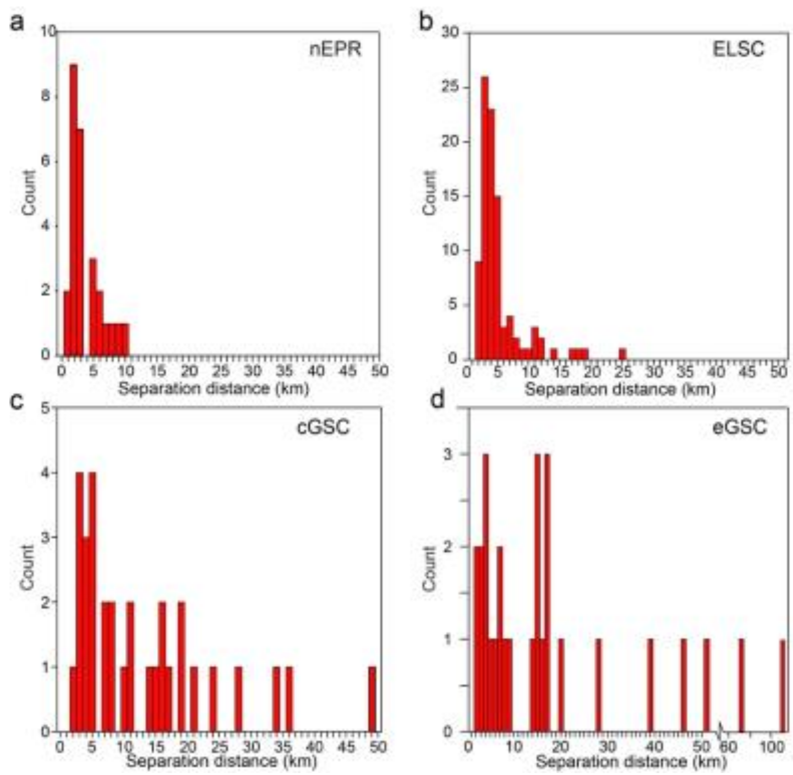

Figure 10

Supplementary Material: Read Me (next page)

Site type	ORP only	start long	start lat	end long	end lat	path (km)	separation end to start (km)

The four data tabs in this worksheet describe the character, location, and extent of all discharge sites determined from the hydrothermal plumes observed in each ridge section.

Column A: Site type, the primary variable, NTU (optical) or ORP (oxidation-reduction potential) used to define the site. Most sites have both NTU and ORP anomalies.
Column B: ORP-only, sites where an NTU plume signal was absent or very weak.
Column C: Start Long, the beginning longitude of the plume anomaly path along a tow track.
Column D: Start Lat, the beginning latitude of the plume anomaly path along a tow track.
Column E: End Long, the ending longitude of the plume anomaly path along a tow track.
Column F: End Lat, the ending latitude of the plume anomaly path along a tow track.
Column G: Path, the distance (km) along the path length of each site.
Column H: Separation, the distance (km) between the end of the previous site and the beginning of the next site.

Supplementary Material: ELSC (next 3 pages)

Site type	ORP only	start long	start lat	end long	end lat	path km	separation end to start km
ORP	ORP only	-175.9695	-19.5629	-175.9763	-19.5977	3.93	
NTU		-175.9889	-19.6331	-175.9970	-19.6650	3.64	4.2
ORP	ORP only	-175.9889	-19.6332	-175.9921	-19.6455	1.41	3.6
NTU		-175.9992	-19.6740	-176.0125	-19.7221	5.52	3.3
ORP		-175.9928	-19.6743	-175.9932	-19.6761	0.20	5.7
ORP		-175.9995	-19.7003	-176.0001	-19.7024	0.24	2.8
ORP	ORP only	-176.0142	-19.7300	-176.0145	-19.7318	0.20	3.4
ORP		-176.0187	-19.7459	-176.0193	-19.7469	0.13	1.6
NTU		-176.0231	-19.7570	-176.0253	-19.7650	0.92	1.2
ORP		-176.0361	-19.8009	-176.0424	-19.8197	2.19	4.1
NTU		-176.0368	-19.8031	-176.0395	-19.8110	0.93	1.9
ORP		-176.0400	-19.8301	-176.0403	-19.8309	0.09	2.1
ORP		-176.0523	-19.8673	-176.0529	-19.8687	0.17	4.2
ORP		-176.0723	-19.9075	-176.0728	-19.9090	0.18	4.8
NTU		-176.0778	-19.9241	-176.0830	-19.9370	1.54	1.8
NTU		-176.0788	-19.9521	-176.0801	-19.9601	0.90	1.7
ORP	ORP only	-176.1098	-19.9981	-176.1205	-20.0249	3.18	5.2
NTU		-176.1112	-20.0020	-176.1367	-20.0730	8.33	2.7
ORP		-176.1076	-20.0083	-176.1219	-20.0445	4.29	7.8
NTU		-176.1076	-20.0083	-176.1432	-20.1250	13.50	4.3
ORP		-176.1239	-20.0332	-176.1263	-20.0399	0.78	10.4
ORP		-176.1346	-20.0657	-176.1348	-20.0663	0.08	3.0
NTU		-176.1382	-20.0901	-176.1035	-20.1350	6.17	2.7
NTU		-176.1246	-20.2730	-176.1255	-20.2800	0.78	15.5
NTU		-176.1358	-20.3180	-176.1458	-20.3520	3.92	4.4
NTU		-176.1410	-20.3200	-176.1475	-20.3371	2.01	3.6
NTU		-176.1488	-20.3610	-176.1662	-20.4210	6.92	2.7
NTU		-176.1616	-20.3870	-176.1515	-20.4291	4.79	3.8
ORP		-176.1617	-20.3906	-176.1598	-20.4037	1.46	4.4
NTU		-176.1711	-20.4350	-176.1807	-20.4611	3.07	3.7
NTU		-176.1697	-20.6201	-176.1762	-20.6631	4.83	17.7
ORP		-176.1702	-20.6367	-176.1727	-20.6497	1.47	3.0
ORP		-176.1788	-20.6719	-176.1792	-20.6729	0.12	2.5
NTU		-176.1770	-20.6870	-176.1779	-20.7250	4.23	1.6
ORP		-176.1768	-20.6887	-176.1761	-20.6941	0.60	4.0
ORP		-176.1878	-20.7016	-176.1886	-20.7046	0.34	1.5
NTU		-176.1839	-20.7540	-176.1987	-20.8050	5.88	5.5
ORP		-176.1843	-20.7560	-176.1852	-20.7604	0.50	5.7
ORP		-176.2153	-20.8547	-176.2188	-20.8746	2.25	10.9
ORP		-176.2117	-20.8659	-176.2124	-20.8701	0.47	1.2
NTU		-176.2236	-20.8970	-176.2344	-20.9250	3.31	3.2
NTU		-176.2206	-20.9060	-176.2277	-20.9230	2.03	2.6
ORP	ORP only	-176.2367	-20.9510	-176.2372	-20.9525	0.17	3.2
NTU		-176.2474	-20.9850	-176.2559	-21.0121	3.13	3.8
ORP		-176.2493	-20.9912	-176.2498	-20.9925	0.15	2.4

NTU		-176.2842	-21.0881	-176.2935	-21.1060	2.22	11.2
NTU		-176.3408	-21.2562	-176.3463	-21.2790	2.60	17.4
ORP		-176.3431	-21.2673	-176.3443	-21.2720	0.54	1.3
NTU		-176.3552	-21.2991	-176.3619	-21.3201	2.43	3.2
NTU		-176.3678	-21.3341	-176.3698	-21.3411	0.80	1.7
ORP	ORP only	-176.3694	-21.4025	-176.3693	-21.4052	0.30	6.8
ORP		-176.3833	-21.4040	-176.3840	-21.4082	0.47	1.5
ORP		-176.3848	-21.4229	-176.3814	-21.4293	0.79	1.6
ORP	ORP only	-176.3869	-21.4891	-176.3883	-21.4937	0.53	6.7
NTU		-176.4428	-21.7031	-176.4561	-21.7410	4.44	23.9
NTU		-176.4574	-21.7270	-176.4643	-21.7480	2.44	1.6
ORP		-176.4520	-21.7295	-176.4546	-21.7368	0.86	2.4
ORP	ORP only	-176.4792	-21.8210	-176.4797	-21.8240	0.34	9.7
NTU		-176.4966	-21.8540	-176.5339	-21.9341	9.70	3.8
ORP		-176.4996	-21.8595	-176.5037	-21.8671	0.95	9.0
ORP		-176.5197	-21.9039	-176.5208	-21.9063	0.29	4.4
ORP		-176.5296	-21.9129	-176.5323	-21.9181	0.65	1.2
ORP		-176.5429	-21.9402	-176.5477	-21.9502	1.22	2.7
ORP		-176.5514	-21.9730	-176.5516	-21.9736	0.07	2.6
ORP		-176.5601	-21.9786	-176.5619	-21.9820	0.42	1.0
ORP	ORP only	-176.5718	-22.0021	-176.5721	-22.0028	0.08	2.5
NTU		-176.5959	-22.0920	-176.5964	-22.1202	3.13	10.2
NTU		-176.6106	-22.1430	-176.6068	-22.1621	2.15	2.9
NTU		-176.6004	-22.1441	-176.6121	-22.2030	6.67	2.1
NTU		-176.6068	-22.1621	-176.6049	-22.1810	2.12	4.6
ORP		-176.6064	-22.1644	-176.6053	-22.1713	0.77	1.9
ORP		-176.6194	-22.1874	-176.6139	-22.1635	2.72	2.3
ORP		-176.6263	-22.1920	-176.6235	-22.1808	1.28	3.4
ORP		-176.6105	-22.1947	-176.6107	-22.1958	0.12	2.0
ORP		-176.6232	-22.2022	-176.6220	-22.1975	0.54	1.5
ORP		-176.6307	-22.2101	-176.6302	-22.2080	0.23	1.7
ORP		-176.6090	-22.2116	-176.6095	-22.2136	0.24	2.2
ORP		-176.6168	-22.2518	-176.6170	-22.2524	0.07	4.3
ORP		-176.6245	-22.2729	-176.6251	-22.2742	0.15	2.4
ORP		-176.6382	-22.2856	-176.6374	-22.2843	0.17	1.9
ORP		-176.6266	-22.2904	-176.6293	-22.2936	0.45	1.3
ORP		-176.6513	-22.3439	-176.6572	-22.3559	1.47	6.0
ORP	ORP only	-176.6672	-22.3515	-176.6703	-22.3603	1.03	1.1
ORP	ORP only	-176.6697	-22.3873	-176.6708	-22.3913	0.46	3.0
ORP	ORP only	-176.6906	-22.4109	-176.6883	-22.4026	0.95	3.0
ORP	ORP only	-176.6793	-22.4303	-176.6796	-22.4314	0.13	3.2
ORP	ORP only	-176.6991	-22.4419	-176.6980	-22.4378	0.47	2.3
NTU		-176.6904	-22.4556	-176.6922	-22.4621	0.74	2.1
ORP	ORP only	-176.6993	-22.4847	-176.6998	-22.4862	0.18	2.6
ORP	ORP only	-176.7046	-22.5004	-176.7067	-22.5066	0.72	1.7
ORP	ORP only	-176.7109	-22.5155	-176.7096	-22.5020	1.50	1.1
ORP	ORP only	-176.7096	-22.5180	-176.7104	-22.5230	0.56	1.8
ORP	ORP only	-176.7189	-22.5308	-176.7167	-22.5159	1.67	1.2

ORP	ORP only	-176.7211	-22.6295	-176.7212	-22.6299	0.05	12.6
ORP	ORP only	-176.7303	-22.6554	-176.7310	-22.6572	0.21	3.0

	95	21
%ORP only		22.11%

Supplementary Material: Central GSC (next page)

Site type	ORP only	start long	start lat	end long	end lat	path km	separation end to start km
ORP	ORP only	-94.8122	2.5982	-94.8118	2.5981	0.04	
NTU		-94.784036	2.5979914	-94.766068	2.5940715	2.04	3.09
ORP	ORP only	-94.69594	2.583728	-94.69562	2.583684	0.04	7.87
ORP	ORP only	-94.39509	2.541	-94.39286	2.5407	0.25	33.72
ORP		-94.3607	2.5368	-94.36003	2.5367	0.08	3.60
ORP	ORP only	-94.14821	2.540382	-94.14716	2.540372	0.12	23.53
ORP		-94.07506	2.526671	-94.07565	2.526735	0.07	8.15
ORP		-94.02806	2.53013	-94.0168	2.527521	1.28	5.30
ORP	ORP only	-93.77059	2.497341	-93.76824	2.497066	0.26	27.56
NTU		-93.725004	2.499173	-93.69503	2.49402817	3.38	4.81
ORP	ORP only	-93.62773	2.473917	-93.62275	2.473076	0.56	7.80
ORP	ORP only	-93.49093	2.45105	-93.48327	2.449721	0.86	14.85
ORP	ORP only	-93.34499	2.436285	-93.34129	2.435176	0.43	15.43
ORP	ORP only	-93.24766	2.373202	-93.24732	2.372838	0.06	12.48
ORP	ORP only	-92.92464	2.275475	-92.92107	2.274649	0.41	37.45
ORP	ORP only	-92.47877	2.17675	-92.47826	2.176664	0.06	50.34
ORP	ORP only	-92.33104	2.144968	-92.32803	2.144514	0.34	16.73
ORP	ORP only	-92.30253	2.138847	-92.2989	2.13746	0.43	2.90
NTU		-92.125039	2.0934953	-92.120099	2.094833	0.57	19.93
ORP	ORP only	-92.00587	2.114698	-91.99743	2.112971	0.96	12.88
NTU		-91.960043	2.108895	-91.810101	2.080225	16.96	4.18
ORP		-91.93715	2.1052	-91.82462	2.0838	12.73	14.39
ORP		-91.93077	2.099799	-91.8722	2.09058	6.59	11.93
NTU		-91.762057	2.0551103	-91.755053	2.05451325	0.78	12.86
NTU		-91.74502	2.0548848	-91.732045	2.05295392	1.46	1.12
NTU		-91.580033	2.0357678	-91.550404	2.015336	4.00	17.00
ORP		-91.39336	1.9684	-91.39311	1.9683	0.03	18.22
NTU		-91.344062	1.9422046	-91.340037	1.94084658	0.47	6.17
ORP		-91.29489	1.924579	-91.29469	1.924525	0.02	5.33
NTU		-91.23501	1.9053398	-91.230019	1.90519875	0.55	6.97
NTU		-91.166033	1.8963216	-91.159051	1.89540792	0.78	7.18
NTU		-91.139046	1.8926555	-91.116033	1.88961563	2.58	2.24
NTU		-91.080021	1.8840477	-91.060125	1.879215	2.28	4.05
33	14						
%ORP only	42.42%						

Supplementary Material: Eastern GSC (next page)

Site type	ORP only	start long	start lat	end long	end lat	path km	separation end to start km
ORP		-90.61024	1.0067	-90.60632	1.0037	0.55	
ORP		-90.55598	0.9566	-90.55253	0.95513	0.42	7.67
ORP	ORP only	-90.21387	0.8995	-90.21304	0.89937	0.09	38.16
ORP	ORP only	-90.04287	0.8706	-90.0417	0.87041	0.13	19.19
ORP	ORP only	-89.63824	0.82294	-89.63725	0.82287	0.11	45.17
NTU		-89.01758	0.8012562	-89.00416	0.800068	1.50	68.94
ORP		-89.00835	0.8004344	-89.00631	0.800256	0.23	0.47
ORP		-88.97551	0.7974662	-88.97507	0.7974259	0.05	3.44
ORP		-88.91617	0.7920215	-88.91594	0.7920001	0.03	6.58
ORP	ORP only	-88.77535	0.7758037	-88.77267	0.7754748	0.30	15.73
ORP		-88.7087	0.7676573	-88.70002	0.7665949	0.97	7.17
ORP		-88.45478	0.7491794	-88.45342	0.7490821	0.15	27.34
ORP		-88.30981	0.7373688	-88.30909	0.7373071	0.08	16.02
ORP		-88.18001	0.7258061	-88.17894	0.7257102	0.12	14.41
ORP		-87.9407	0.7227938	-87.94034	0.7227792	0.04	26.49
NTU		-87.89943	0.7209066	-87.89229	0.720565	0.79	4.55
NTU		-87.85006	0.7191902	-87.84362	0.7190921	0.72	4.70
ORP	ORP only	-87.72626	0.7144177	-87.72455	0.7142151	0.19	13.06
ORP	ORP only	-87.6961	0.7106611	-87.69503	0.7105229	0.12	3.19
ORP	ORP only	-86.70626	0.8494646	-86.70292	0.8490965	0.37	111.02
ORP	ORP only	-86.25557	0.8082622	-86.25457	0.8081654	0.11	49.94
ORP	ORP only	-86.10949	0.7911868	-86.10835	0.7910464	0.13	16.24
ORP		-86.08905	0.788678	-86.08714	0.7884441	0.21	2.16
ORP		-85.95204	0.7731207	-85.9514	0.7730515	0.07	15.12
NTU		-85.92238	0.7699218	-85.91917	0.7695753	0.36	3.25
ORP		-85.91238	0.7688277	-85.90965	0.7685295	0.31	0.76
ORP		-85.89625	0.7670861	-85.89561	0.7670171	0.07	1.50
ORP		-85.87332	0.7646359	-85.87136	0.7644271	0.22	2.49
28	9						
%ORP only	32.14%						

Supplementary Material: Northern EPR (next page)

Site type	ORP only	start long	start lat	end long	end lat	path km	separation end to start km
NTU		-104.1981	9.1221	-104.2035	9.1521	3.39	
ORP		-104.2054	9.1662	-104.2060	9.1707	0.50	1.58
ORP	ORP only	-104.2091	9.1847	-104.2095	9.1870	0.27	1.59
ORP		-104.2155	9.2473	-104.2162	9.2521	0.54	6.73
ORP		-104.2188	9.3155	-104.2182	9.3162	0.09	7.06
ORP		-104.2215	9.3288	-104.2218	9.3324	0.41	1.44
ORP		-104.2198	9.3774	-104.2205	9.3833	0.66	5.00
NTU		-104.2246	9.3993	-104.2254	9.3999	0.11	1.84
ORP		-104.2282	9.4192	-104.2291	9.4257	0.73	2.16
ORP		-104.2329	9.4453	-104.2331	9.4469	0.18	2.22
NTU		-104.2357	9.4592	-104.2358	9.4598	0.07	1.40
ORP		-104.2392	9.4817	-104.2397	9.4875	0.65	2.46
ORP		-104.2453	9.5089	-104.2445	9.5090	0.09	2.46
NTU		-104.2503	9.5782	-104.2510	9.5834	0.58	7.73
NTU		-104.2554	9.6184	-104.2599	9.6490	3.44	3.92
ORP		-104.2556	9.6190	-104.2634	9.6715	5.91	3.37
NTU		-104.2602	9.6573	-104.2657	9.6695	1.49	1.63
ORP		-104.2651	9.6808	-104.2651	9.6821	0.14	1.26
ORP		-104.2702	9.7053	-104.2705	9.7067	0.16	2.64
ORP		-104.2736	9.7283	-104.2743	9.7358	0.84	2.42
ORP		-104.2876	9.8114	-104.2887	9.8208	1.05	8.53
ORP		-104.2912	9.8378	-104.2913	9.8386	0.09	1.91
ORP		-104.2926	9.8475	-104.2929	9.8490	0.17	1.00
NTU		-104.2984	9.8919	-104.2998	9.9019	1.12	4.80
NTU		-104.3159	9.9779	-104.3194	9.9852	0.89	8.64
ORP		-104.3189	9.9955	-104.3190	9.9963	0.09	1.14
NTU		-104.3213	10.0057	-104.3210	10.0058	0.03	1.08
27	1						
%ORP only	3.70%						